



Ultrabroadband suppression of mid-infrared reflection losses of a layered semiconductor by nanopatterning with a focused ion beam

MATTHIAS HAGNER,^{1,2} PHILIPP SULZER,^{1,2}  ANDREAS LIEHL,¹ MORITZ CIMANDER,¹ HANNES KEMPF,¹ ANNIKA BITZER,¹ ALEXA HERTER,¹ AND ALFRED LEITENSTORFER^{1,*}

¹Department of Physics and Center for Applied Photonics, University of Konstanz, D-78457 Konstanz, Germany

²These authors contributed equally to this work

*Alfred.Leitenstorfer@uni-konstanz.de

Abstract: Moth-eye structures are patterned onto gallium selenide surfaces with sub-micrometer precision. In this way, Fresnel reflection losses are suppressed to below one percent within an ultrabroad optical bandwidth from 15 to 65 THz. We tune the geometry by rigorous coupled-wave analysis. Subsequently, ablation with a Ga⁺ ion beam serves to write optimized structures in areas covering 30 by 30 μm. The benefits are demonstrated via optical rectification of femtosecond laser pulses under tight focusing, resulting in emission of phase-stable transients in the mid-infrared. We analyze the performance of antireflection coating directly in the time domain by ultrabroadband electro-optic sampling.

© 2021 Optical Society of America under the terms of the [OSA Open Access Publishing Agreement](#)

1. Introduction

Emission of phase-stable mid-infrared transients results from optical rectification [1] or ultrafast transport processes [2] driven by few-femtosecond laser pulses. Subsequently, ultrabroadband electro-optic sampling provides direct time-domain access to the electric field traces [2,3]. Owing to its high second-order nonlinearity, strong birefringence and wide transmission window, the layered semiconductor GaSe has found widespread application in this context both as an emitter [4] and detector [5,6]. Over the last two decades, these technologies have enabled time- and phase-resolved mid-infrared spectroscopy of condensed matter, solid-state nanostructures, gases and even biological systems [7–14]. More recently, the control of time-resolved fields in this spectral range has become a cornerstone of the emerging area of time-domain quantum electrodynamics. Interest in this subject has been sparked by the first direct detection of the vacuum fluctuations of the electromagnetic field [15,16]. An increasing body of related studies in both experiment and theory [17–23] is working towards exploring the quantum properties of light with subcycle resolution. Such nonclassical states may be generated via nonlinear interaction of intense femtosecond pulses with dielectric nonlinear media. However, in order to examine their quantum character and to harness it for metrology or spectroscopy, it is of paramount importance to preserve the purity of the nonclassical state while propagating it across the surface of a nonlinear element. Any losses result in admixture of uncorrelated vacuum fluctuations, as typically modelled by the open port of a beamsplitter [24]. The crystals employed for generating and detecting these states are non-resonant in the relevant spectral regions and therefore, reflections at their surfaces constitute the largest threat to quantum applications. For typical specimens, these Fresnel losses can eliminate almost half the field amplitude between emitter and detector, constituting a major challenge for achieving a full quantum tomography in the time domain [25]. In addition, another challenge created by the interface between material and air/vacuum are the echoes spawned by multiple reflections inside the crystal. This effect

becomes especially harmful when filtering in the time domain is performed to isolate relevant contributions, as typically observed in many studies based on field-resolved spectroscopy [26]. Overlap of the echo of an intense pulse with the signal of interest may severely deteriorate the information content. A conventional solution to both problems, i.e. losses and delayed replicas, is provided by antireflection (AR) coatings on the exit and entrance facets of nonlinear elements. However, such coatings are of limited bandwidth and efficiency especially in the mid infrared. In addition, they induce unwanted spectral phases on ultrashort pulses. They also may be challenging to deposit on some important nonlinear materials with two-dimensional layering such as GaSe due to adhesion problems on atomically flat surfaces with strongly different thermal expansion coefficients [27]. An alternative method was recently applied to GaSe surfaces [28]: AR microstructures fabricated by single-pulse femtosecond laser ablation.

In this paper, we present broadband and highly efficient suppression of reflection losses even of cumbersome nonlinear crystals with van-der-Waals-bound layered character: nanostructuring of the surface with a focused-ion beam (FIB) to establish a moth-eye structure [29]. Here, the step-like transition of the linear refractive index at the interface GaSe/air is circumvented. Instead, the effective index experienced by the incident electromagnetic wave changes continuously along the longitudinal direction. As a consequence, Fresnel losses are minimized. This strategy is especially advantageous for the small spot sizes of mid-infrared ultrashort pulses typically employed in the context of time-domain quantum optics. It turns out that our approach suppresses reflections on the GaSe-air interface by orders of magnitude without adding any noticeable spectral phase, therefore preserving the pure quantum character of the emitted transients. Furthermore, FIB milling provides a resolution enabling even smaller structures for application in the near-infrared and visible spectral range. The details of the sample preparation process are discussed in Section 2 and a rigorous theoretical model for the reflection properties of the resulting nanopatterns is presented in Section 3. Section 4 introduces the femtosecond optical setup for characterizing the moth-eye structures and demonstrates their compatibility with ultrasensitive time-domain spectroscopy. It also compares our experimental data with the numerical simulations and with results from recent literature.

2. Manufacturing

Bulk GaSe exhibits a two-dimensional structure of hexagonal atomic trilayers bound by van-der-Waals forces, allowing cleavage only along the (001) planes. While this fact enables the exfoliation of extremely thin samples approaching the few-layer limit [30], it also complicates processing with macroscopic cutting or polishing techniques. To the best of our knowledge, the sole method beyond growth and exfoliation demonstrated to date is cutting or microstructuring via laser ablation [28,31]. Here, we demonstrate that nanostructuring of the surface of a material as anisotropic as GaSe with a resolution substantially below 1 μm is readily possible with FIB. This finding enables us to create moth-eye structures on the surface of a highly efficient layered material for nonlinear optics. The specific dimensions of the structures are determined to allow for strong suppression of reflections of mid-infrared radiation.

We employ a Zeiss Neon 40EsB system equipped with a beam of Ga^+ ions for nanopatterning and a scanning-electron microscope (SEM) for simultaneous process control. Beyond the superior spatial resolution provided by the ion beam, Ga^+ ions also offer the advantage of not introducing additional chemical elements which could act as impurities in the material. At the same time, maximum energy transfer to the Ga atoms of the compound is ensured. The penetration depth of implanted Ga^+ ions is estimated to be 20 nm under our conditions with state-of-the-art stopping and range of ions in matter (SRIM) software. Note that this length scale is much smaller as compared to both the thickness of our nonlinear-optical crystal and thickness of the moths-eye coatings as well as to the mid-infrared wavelengths we are dealing with. Consequently, we do not expect significant influences of the FIB milling process on the performance of the

structures. A schematic arrangement of the two beams is represented in Fig. 1(a). Ga^+ ions are accelerated to 30 keV and focussed onto the GaSe surface for precise ablation. A nanopatterning and visualization engine extends the capabilities of beam guidance, enabling the production of complex structures on a relatively large surface. Essential for patterning moth-eye structures into a GaSe crystal are an adapted milling strategy and a high-resolution ion beam. We achieved the best results employing an ion current of 500 pA corresponding to a beam diameter of approximately 50 nm. During the process, the ion beam is scanned over the sample with 10.000 repetitions to create the desired shapes. We also take into account the nonlinearity between exposure time and milling depth, resulting in an adjusted lateral dose as displayed in Fig. 1(b).

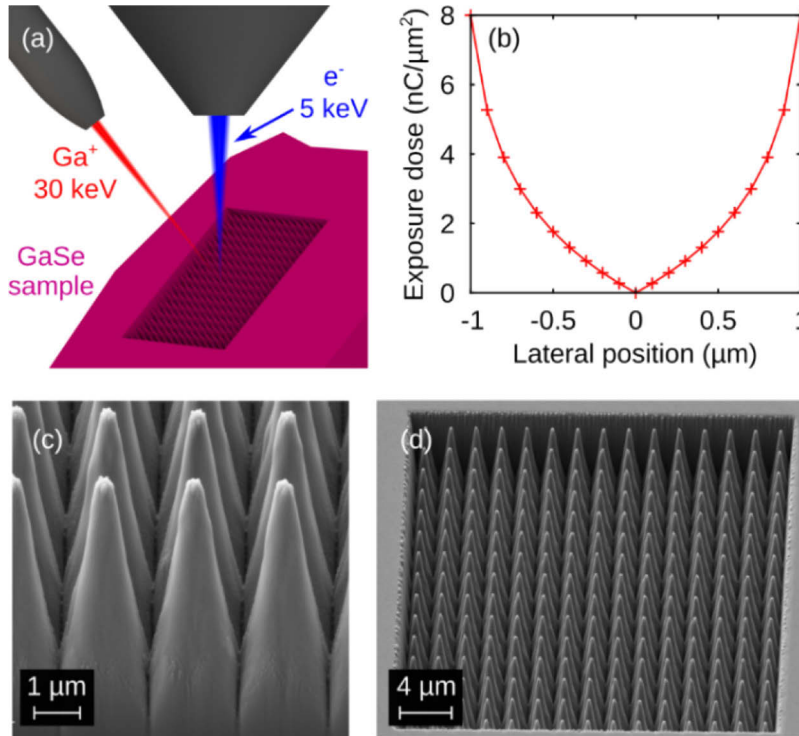


Fig. 1. (a) Schematic of the sample preparation: a Ga^+ ion beam for patterning (red) and the electron beam (blue) are focused onto the GaSe sample (purple). (b) Lateral profile of the exposure dose by the ion beam through the cross section of a single pyramid. (c) High-resolution SEM micrograph of a part of the processed area. (d) SEM overview of the entire periodic structure.

Mechanical drift of the sample position inevitably occurs throughout this process. Therefore, it is crucial to implement an efficient strategy for drift compensation. To this end, markers are written into the substrate with the ion beam in the immediate vicinity of the projected writing field before the actual processing. These markers are recorded every 240 s during the patterning and the drift of the sample is corrected. Figure 1(c) clearly demonstrates the precise and high-resolution processing of the GaSe crystal enabled by the Ga^+ ion beam. To the best of our knowledge, no other technique has so far demonstrated comparable performance in three-dimensional nanopatterning of the surface of a layered material like GaSe. Figure 1(d) displays the entire pattern of a dimension of 30 by 30 μm which took 2 hours of FIB processing time.

3. Simulation

To tailor the reflection and transmission properties of the moth-eye structure in the mid infrared, we apply rigorous coupled-wave analysis (RCWA) [32–34] exploiting the modeling code GD-Calc (Grating Diffraction Calculator, KJ Innovation, U.S.). Figure 2(a) displays a segment of the periodic geometry underlying numerical simulation. It consists of a two-dimensional array of micro-sized pyramids located on top of the crystal surface. Along the optical propagation axis (indicated by the wave vector \mathbf{k}_{THz} and z axis in Fig. 2(a)), the grating structure is split into 32 horizontal slices resulting in staircase-shaped edges. In each layer, the lateral periodicity of the dielectric function is modelled by a Fourier series. Additionally, we apply a Sellmeier equation in order to account for the linear dispersion of GaSe [35]. The RCWA algorithm then solves the Helmholtz equation in each sublayer for plane monochromatic waves under normal incidence while considering the electromagnetic boundary conditions. This step is repeated multiple times with varying wavelengths to map out the frequency dependence of the grating properties. In this way, we obtain the total Fresnel coefficients of the moth-eye structure for both s- and p-polarized inputs. However, since the period of the array is equal in both lateral directions (x- and y-axis), the overall reflection and transmission is independent of polarization.

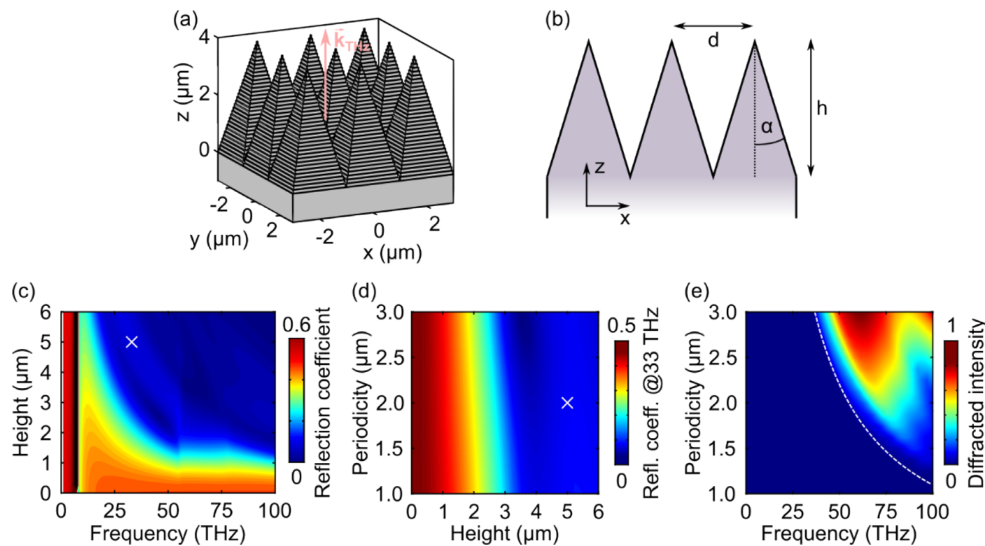


Fig. 2. (a) Three-dimensional model underlying the numerical simulations. The magenta arrow represents the wave vector \mathbf{k}_{THz} of the incoming radiation, indicating normal incidence. (b) Cross section of the structure displayed in panel (a) in the x-z plane at $y = 0$. (c) Amplitude reflection coefficient color-coded versus the depth h of the moth-eye structures and optical frequency at a fixed grating period of $d = 2 \mu\text{m}$. The white cross marks the experimental situation discussed in Fig. 4. (d) Amplitude reflection coefficient at an optical frequency of 33 THz calculated as a function of the periodicity d and etch depth h of the moth-eye grating. The white marker represents the parameters chosen in our experiment. (e) Normalized intensity transferred to higher orders of diffraction color-coded versus frequency and structure periodicity d . The white-dashed line denotes the optical frequency where the wavelength within bulk GaSe equals the grating period.

In order to find the maximum suppression of reflections at the GaSe surface, we now vary the geometrical properties of the structure, i.e. its period d and the height h of the pyramids. Figure 2(b) features a cross section of the structure along the x-z-plane where those quantities are defined. The opening angle α of the pyramids is unambiguously given by $\alpha = \arctan(d/2h)$.

Figure 2(c) then depicts the amplitude reflection coefficient inferred from RCWA as a function of h and optical frequency. The periodicity is fixed at $d = 2 \mu\text{m}$. These results demonstrate that the higher the structures the lower the Fresnel reflection coefficient. Tendentially, the sharper the pyramids are, the smoother the spatial transition of the refractive index becomes, thus resulting in a better performance of the anti-reflection coating. Note that the nanolithographic fabrication process of the gratings developed here limits the aspect ratio $h:d$ to approximately 3:1. In addition, deep etching into the bulk GaSe crystal reduces its effective thickness and consequently the converted power during nonlinear-optical interactions. Thus, we choose a realistic height parameter of $h = 5 \mu\text{m}$.

In the next step, we also vary the periodicity of the grating. Figure 2(d) shows the calculated amplitude reflection coefficient with respect to the geometric parameters d (periodicity) and h (height) at a frequency of 33 THz. Blue and red colors indicate low and high reflection coefficients, respectively. Obviously, the total reflection is only weakly affected by the grating period. The transmitted intensity, in turn, is split into multiple diffraction maxima if the lateral separation exceeds the wavelength of the multi-terahertz radiation. The normalized intensity contained within higher diffraction orders, i.e., within all interference maxima except for the zero-order peak, after transmission through the moth-eye structure is depicted in Fig. 2(e). These results clearly demonstrate that the lower the distance between the pyramids, the higher the cut-off frequency ν_{cut} at which diffraction to higher-order maxima starts to play a role (white dashed line). For $d = 2 \mu\text{m}$, we find $\nu_{\text{cut}} = 55 \text{ THz}$, explaining also the minor discontinuity in the data of Fig. 2(c).

To summarize the results of the RCWA simulations presented in Figs. 2(c-e), our choice of $h = 5 \mu\text{m}$ and $d = 2 \mu\text{m}$ represents a good trade-off between high-quality structuring and minimum Fresnel losses for an ultrabroadband frequency band centered at 33 THz (see also white markers in Figs. 2(c) and 2(d)).

4. Characterization setup and results

We now proceed to demonstrate the viability of these considerations by exploiting a nanostructured sample as a generation crystal (GX) for coherent and phase-locked mid-infrared pulses. The experimental setup is depicted in Fig. 3(a). It is based on a modelocked Er: fiber oscillator and two femtosecond Er: fiber amplifiers [36]. The output of both branches is spectrally broadened in separate highly nonlinear fibers to achieve pulse durations of 10 fs. The pump branch (green solid line, repetition rate of $f_{\text{rep}} = 20 \text{ MHz}$) is centered at 1550 nm. The center of the probe spectrum (blue, $f_{\text{rep}} = 40 \text{ MHz}$) is located at a wavelength of 1200 nm. In the time-domain experiment, pump pulses generate phase-stable mid-infrared transients with frequency content from 10 to 100 THz via intrapulse difference-frequency generation [4]. This output is spatiotemporally superimposed with the probe beam and focused onto the electro-optic detection crystal (EOX). In this way, the electric field transient may be recorded in amplitude and phase via free-space electro-optic sampling [25]. We harness this setup to demonstrate the application of FIB-milled moth-eye structures as an ultrabroadband AR coating on the layered nonlinear material GaSe. Figure 3(b) outlines how the quantitative difference in amplitude between the main transient and its reflection-induced replicas may be exploited to examine the Fresnel reflection coefficients at the emitting side of the GX. When a mid-infrared pulse, depicted as a red solid line, is generated by optical rectification of the pump beam (green pulse in Fig. 3(b)), it propagates through the crystal and is partly reflected at the flat surface (upper half of Fig. 3(b)). An additional reflection on the opposite air-dielectric interface spatially overlaps the replica with the main beam. Subsequently, this pulse is transmitted into the EOX where it generates a delayed signal. The path of the echo is depicted as a red dashed line in Fig. 3(b). In contrast, the spurious delayed signal should be suppressed almost completely if the nanostructuring technique described in Sections 2 and 3 is applied (lower half of Fig. 3(b)). Laterally translating the GX switches the

exiting beam on the GaSe surface from the nanostructured area to the unmodified flat region next to it. This procedure enables straightforward recording of a maximally comparable reference measurement without changes to any additional alignment parameters.

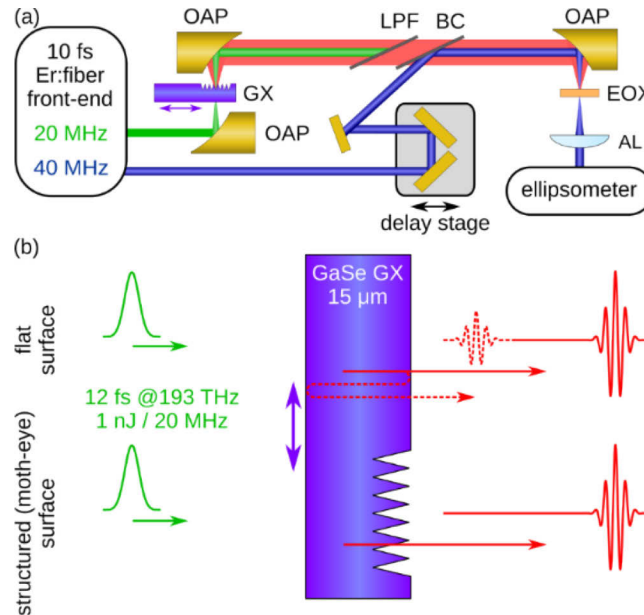


Fig. 3. (a) Sketch of the experimental setup. Femtosecond pump (20 MHz, green) and probe beams (40 MHz, blue) are synthesized by an Er: fiber front-end. The pump pulses generate phase-stable multi-terahertz transients in a nonlinear generation crystal (GX) via optical rectification (path depicted in red). After recollimation, both branches are spatiotemporally overlapped and focused into an electro-optic crystal (EOX). A variable optical delay stage scans the delay t_D between pump and probe. The field-induced polarization change is then recorded as an electro-optic signal by an ellipsometer. LPF: optical low-pass filter (150 μm of GaSb). BC: beam combiner (500 μm of Si). OAP: off-axis parabolic mirrors (Au coated). AL: achromatic lens. (b) A near-infrared pump pulse (green) generates a few-cycle multi-terahertz pulse in the GaSe GX and propagates to the end facet of the crystal. Top: Reflection on the native surface of the GX leads to a replica (dashed line) of the main pulse (solid line), delayed by the optical path length corresponding to twice the thickness of the GX. Bottom: Reflection is eliminated if the pulse hits the structured end facet.

In the following, we present and analyze data recorded using the setup and principles described above. Electro-optic signals taken with a 15- μm -thick GaSe GX are depicted in Fig. 4(a). The top panel displays a transient propagated through a flat GaSe surface as a blue solid line. The data features three separate waveforms. The first one is centered around a relative delay time of $t_D = 0$. It is attributed to the fundamental multi-terahertz pulse generated in the GX. This signal will be denoted as the main transient below. It is followed by a second waveform which originates from reflections inside the GX and will be called the reflected transient. The additional replica located at $t_D = 325$ fs is due to Fresnel reflections within the EOX. The time between the main and reflected transients amount to 275 fs and their relative field amplitude is 22%. These values are consistent with two additional reflections on GaSe-air interfaces with a refractive-index contrast of 2.72. Also, the delay corresponds to twice the geometrical thickness and a group refractive index of 2.75 [35]. In contrast, the red solid line in the lower panel of Fig. 4(a) features data recorded with the multi-terahertz beam propagating through the nanostructured surface. It exhibits a reflected transient with a maximum amplitude on the order of only a few percent of the

main transient. The drastic decrease in peak amplitude of the echo already indicates an excellent performance of the structures.

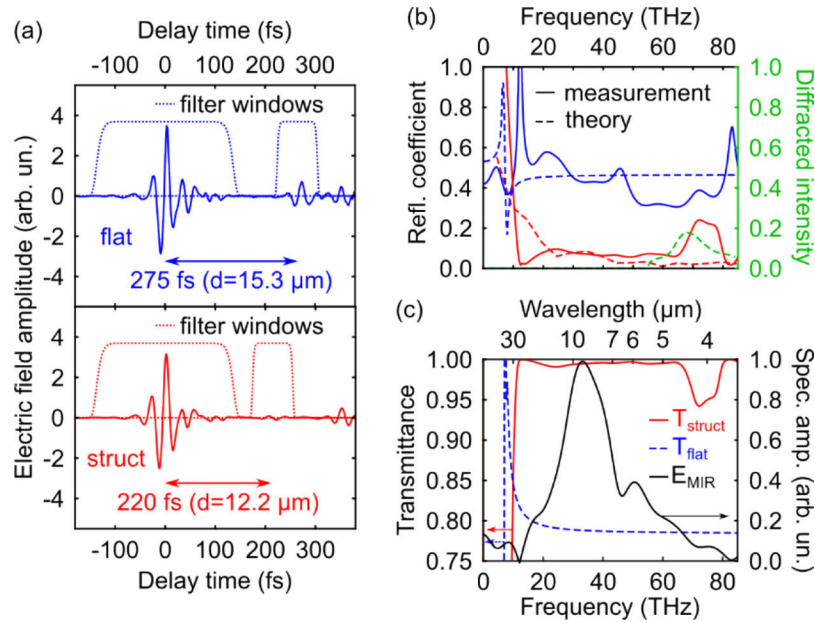


Fig. 4. (a) Electric field transients recorded illuminating a native (top panel, blue solid line) or structured (bottom, red) section of the GX. The dotted lines indicate the filtering windows used for Fourier transform. (b) Solid lines display the reflection coefficients as a function of frequency inferred from the transients and filter windows depicted in (a) with blue representing a flat, and red representing a structured surface of the GX. The dashed lines indicate the prediction from either Fresnel's equations (blue, flat GX) or the numerical simulations displayed in Fig. 2 (red, nanostructured GX). The green dashed line represents the calculated relative intensity in the higher orders of diffraction (horizontal slice of Fig. 2(e) at a periodicity of $d = 2 \mu\text{m}$). (c) Intensity transmittance as a function of frequency and wavelength. The solid red line depicts the data corresponding to the nanostructure and the dashed blue line shows the expected transmittance for a flat GaSe surface. The spectral field amplitude of the main transients depicted in panel (a) is indicated as a black line.

The temporal offset between both waveforms has decreased to 220 fs. This time delay corresponds to an optical path length of $12 \mu\text{m}$, as expected due to the change in effective thickness after nanostructuring via FIB. This fact also shortens the interaction length during optical rectification. Thus, the electric field amplitude of the main transient reduces as well. However, this effect is canceled by the enhanced transmission of electromagnetic intensity at the moth-eye surface. Therefore, the electro-optic signals displayed in the top and bottom panel of Fig. 4(a) exhibit similar amplitudes. Note also that the second replica centered around a relative delay of $t_D = 325 \text{ fs}$ is nearly identical to the measurement presented in the top panel since the EOX has not been modified.

To investigate the properties of our nanostructure AR coating more quantitatively, we first compute the spectrally integrated field reflection coefficient directly from the peak electric field amplitudes of main $E_{\text{peak}}^{\text{main}}$ and reflected transients $E_{\text{peak}}^{\text{refl}}$. These values are related to the field reflectivity coefficients for the flat r_{flat} and structured surface r_{struct} as follows: $E_{\text{peak}}^{\text{refl}} = E_{\text{peak}}^{\text{main}} r_{\text{flat}} r_{\text{struct}}$. Using the literature values for the flat surface reflection [35] and the data displayed in Fig. 4(a), we find a value of $r_{\text{struct}} \approx 0.078$. Consequently, the intensity reflection coefficient becomes $R_{\text{struct}} = |r_{\text{struct}}|^2 = |E_{\text{peak}}^{\text{refl}} / (E_{\text{peak}}^{\text{main}} r_{\text{flat}})|^2 \approx 0.006$. This result must be understood

as an average reflectivity weighed by the spectral intensity of the MIR transients. We analyze this performance further by separating the main and reflected transients using supergaussian filter functions as marked by the dashed lines in Fig. 4(a). The resulting segments are then Fourier transformed. Afterwards, we determine the frequency-dependent reflection coefficients by dividing the resulting spectra of main and reflected transients emitted through the flat GaSe surface. This algorithm is applied separately to both measurements depicted in the upper and lower panels of Fig. 4(a). The result is displayed in Fig. 4(b). A blue solid line represents the case where the multi-terahertz transient propagates through the flat exit surface of the GX. This graph agrees well with the dash-dotted blue line depicting the result of Fresnel's equations for normal incidence with literature values for the refractive index of GaSe [35]. In analogy, the red solid line in Fig. 4(b) represents the amplitude reflection coefficient of the moth-eye structures, revealing a drastic reduction in reflectivity. Specifically, the field coefficients remain in the few-percent range over a large bandwidth. The dashed red line indicates the corresponding part of simulation results from Fig. 2(a). Interestingly, the measured data even outperforms the level predicted by our model described in Section 2 for frequencies between 10 and 20 THz. This observation may be explained by the fact that the focused ion beam penetrates the GaSe specimen deeper than intended, as it is clearly visible when comparing Figs. 2(a) and 1(c): an increase of the height of the structure redshifts the low-frequency onset of residual reflections (see Fig. 2(b)).

To enable direct comparison with typical characterizations of antireflective coatings, we also depict the intensity transmission spectra for both flat (blue dashed line) and nanostructured (red solid line) exit facets at the GX in Fig. 4(c). They are calculated from the field reflectivity in Fig. 4(b) assuming negligible absorption, i.e. $T = 1 - |r|^2$. Values above 0.99 are observed over a bandwidth of multiple octaves spanning from 15 to 65 THz. This interval corresponds to a range from 4.5 to 25 μm in terms of wavelength.

5. Conclusion

In summary, we have demonstrated high-quality fabrication of moth-eye nanostructures on the layered material GaSe via focused-ion-beam milling. This achievement establishes a viable route to arbitrarily modify the surfaces of this highly nonlinear optical medium down to the nanoscale. The performance of our approach is remarkable considering the layered and therefore highly anisotropic character of this compound. Such a structure establishes an ultra-broadband AR coating. Reduction of the intensity reflectance by two orders of magnitude is achieved over a broad spectral range from 15 to 65 THz (corresponding to wavelengths between 4.5 and 25 μm). Consequently, we have provided an ultrabroadband solution for the problem of substantial reflection losses to the nascent topics of time-domain quantum optics and ultrasensitive field-resolved spectroscopy in the mid infrared.

Funding. Deutsche Forschungsgemeinschaft (425217212 – SFB 1432).

Disclosures. The authors declare no conflicts of interest.

Data availability. Data underlying the results presented in this paper are not publicly available at this time but may be obtained from the authors upon reasonable request.

References

1. A. Bonvalet, M. Joffre, J. L. Martin, and A. Migus, "Generation of ultrabroadband femtosecond pulses in the mid-infrared by optical rectification of 15 fs light pulses at 100 MHz repetition rate," *Appl. Phys. Lett.* **67**(20), 2907–2909 (1995).
2. A. Leitenstorfer, S. Hunsche, J. Shah, M. C. Nuss, and W. H. Knox, "Detectors and sources for ultrabroadband electro-optic sampling: Experiment and theory," *Appl. Phys. Lett.* **74**(11), 1516–1518 (1999).
3. Q. Wu and X.-C. Zhang, "Free-space electro-optics sampling of mid-infrared pulses," *Appl. Phys. Lett.* **71**(10), 1285–1286 (1997).
4. R. Huber, A. Brodschelm, F. Tauser, and A. Leitenstorfer, "Generation and field-resolved detection of femtosecond electromagnetic pulses tunable up to 41 THz," *Appl. Phys. Lett.* **76**(22), 3191–3193 (2000).

5. K. Liu, J. Xu, and X.-C. Zhang, "GaSe crystals for broadband terahertz wave detection," *Appl. Phys. Lett.* **85**(6), 863–865 (2004).
6. C. Kübler, R. Huber, S. Tübel, and A. Leitenstorfer, "Ultrabroadband detection of multi-terahertz field transients with GaSe electro-optic sensors: Approaching the near infrared," *Appl. Phys. Lett.* **85**(16), 3360–3362 (2004).
7. R. Huber, F. Tauser, A. Brodschelm, M. Bichler, G. Abstreiter, and A. Leitenstorfer, "How many-particle interactions develop after ultrafast excitation of an electron-hole plasma," *Nature* **414**(6861), 286–289 (2001).
8. M. Tonouchi, "Cutting-edge terahertz technology," *Nat. Photonics* **1**(2), 97–105 (2007).
9. P. U. Jepsen, D. G. Cooke, and M. Koch, "Terahertz spectroscopy and imaging – Modern techniques and applications," *Laser Photonics Rev.* **5**(1), 124–166 (2011).
10. M. Först, C. Manzoni, S. Kaiser, Y. Tomioka, Y. Tokura, R. Merlin, and A. Cavalleri, "Nonlinear phononics as an ultrafast route to lattice control," *Nat. Phys.* **7**(11), 854–856 (2011).
11. K. W. Kim, A. Pashkin, H. Schäfer, M. Beyer, M. Porer, T. Wolf, C. Bernhard, J. Demsar, R. Huber, and A. Leitenstorfer, "Ultrafast transient generation of spin-density-wave order in the normal state of BaFe₂As₂ driven by coherent lattice vibrations," *Nat. Mater.* **11**(6), 497–501 (2012).
12. T. Kampfrath, M. Battiato, P. Maldonado, G. Eilers, J. Nötzold, S. Mährlein, V. Zbarsky, F. Freimuth, Y. Mokrousov, S. Blügel, M. Wolf, I. Radu, P. M. Oppeneer, and M. Münzenberg, "Terahertz spin current pulses controlled by magnetic heterostructures," *Nat. Nanotechnol.* **8**(4), 256–260 (2013).
13. T. L. Cocker, D. Peller, P. Yu, J. Repp, and R. Huber, "Tracking the ultrafast motion of a single molecule by femtosecond orbital imaging," *Nature* **539**(7628), 263–267 (2016).
14. A. von Hoegen, R. Mankowsky, M. Fechner, M. Först, and A. Cavalleri, "Probing the interatomic potential of solids with strong-field nonlinear phononics," *Nature* **555**(7694), 79–82 (2018).
15. C. Riek, D. V. Seletskiy, A. S. Moskalenko, J. F. Schmidt, P. Krauspe, S. Eckart, S. Eggert, G. Burkard, and A. Leitenstorfer, "Direct sampling of electric-field vacuum fluctuations," *Science* **350**(6259), 420–423 (2015).
16. A. S. Moskalenko, C. Riek, D. V. Seletskiy, G. Burkard, and A. Leitenstorfer, "Paraxial Theory of Direct Electro-optic Sampling of the Quantum Vacuum," *Phys. Rev. Lett.* **115**(26), 263601 (2015).
17. I.-C. Benea-Chelmus, C. Bonzon, C. Maissen, G. Scalari, M. Beck, and J. Faist, "Subcycle measurement of intensity correlations in the terahertz frequency range," *Phys. Rev. A* **93**(4), 043812 (2016).
18. C. Riek, P. Sulzer, M. Seeger, A. S. Moskalenko, G. Burkard, D. V. Seletskiy, and A. Leitenstorfer, "Subcycle quantum electrodynamics," *Nature* **541**(7637), 376–379 (2017).
19. I.-C. Benea-Chelmus, F. F. Settembrini, G. Scalari, and J. Faist, "Electric field correlation measurements on the electromagnetic vacuum state," *Nature* **568**(7751), 202–206 (2019).
20. M. Kizmann, T. L. de M. Guedes, D. V. Seletskiy, A. S. Moskalenko, A. Leitenstorfer, and G. Burkard, "Subcycle squeezing of light from a time flow perspective," *Nat. Phys.* **15**(9), 960–966 (2019).
21. T. L. M. Guedes, M. Kizmann, D. V. Seletskiy, A. Leitenstorfer, G. Burkard, and A. S. Moskalenko, "Spectra of Ultrabroadband Squeezed Pulses and the Finite-Time Unruh-Davies Effect," *Phys. Rev. Lett.* **122**(5), 053604 (2019).
22. S. De Liberato, "Electro-optical sampling of quantum vacuum fluctuations in dispersive dielectrics," *Phys. Rev. A* **100**(3), 031801 (2019).
23. F. Lindel, R. Bennett, and S. Y. Buhmann, "Theory of polaritonic quantum-vacuum detection," *Phys. Rev. A* **102**(4), 041701 (2020).
24. R. Loudon, *The Quantum Theory of Light* (Oxford University, 1973).
25. P. Sulzer, K. Oguchi, J. Huster, M. Kizmann, T. L. M. Guedes, A. Liehl, C. Beckh, A. S. Moskalenko, G. Burkard, D. V. Seletskiy, and A. Leitenstorfer, "Determination of the electric field and its Hilbert transform in femtosecond electro-optic sampling," *Phys. Rev. A* **101**(3), 033821 (2020).
26. I. Pupeza, M. Huber, M. Trubetskov, W. Schweinberger, S. A. Hussain, C. Hofer, K. Fritsch, M. Poetzlberger, L. Vamos, E. Fill, T. Amotchkina, K. V. Kepesidis, A. Apolonski, N. Karpowicz, V. Pervak, O. Pronin, F. Fleischmann, A. Azzeer, M. Žigman, and F. Krausz, "Field-resolved infrared spectroscopy of biological systems," *Nature* **577**(7788), 52–59 (2020).
27. R. A. Redkin, D. A. Kobtsev, S. A. Bereznaya, Z. V. Korotchenko, Y. S. Sarkisov, T. A. Mihaylov, and S. Y. Sarkisov, "GaSe crystals with antireflection coatings for terahertz generation," *Mater. Res. Express* **6**(12), 126201 (2019).
28. A. A. Bushunov, A. A. Teslenko, M. K. Tarabrin, V. A. Lazarev, L. I. Isaenko, A. P. Eliseev, and S. I. Lobanov, "Fabrication of antireflection microstructures on the surface of GaSe crystal by single-pulse femtosecond laser ablation," *Opt. Lett.* **45**(21), 5994–5997 (2020).
29. C. G. Bernhard, "Structural and functional adaptation in a visual system," *Endeavour* **26**(98), 79–84 (1967).
30. A. Budweg, D. Yadav, A. Grupp, A. Leitenstorfer, M. Trushin, F. Pauly, and D. Brida, "Control of excitonic absorption by thickness variation in few-layer GaSe," *Phys. Rev. B* **100**(4), 045404 (2019).
31. D. Cheshev, P. D. Rodriguez, A. Matkovic, A. Ruban, J.-J. Chen, and E. Sheremet, "Patterning GaSe by High-Powered Laser Beams," *ACS Omega* **5**(17), 10183–10190 (2020).
32. M. G. Moharam and T. K. Gaylord, "Rigorous coupled-wave analysis of planar-grating diffraction," *J. Opt. Soc. Am.* **71**(7), 811–818 (1981).
33. K. Han and C.-H. Chang, "Numerical Modeling of Sub-Wavelength Anti-Reflective Structures for Solar Module Applications," *Nanomaterials* **4**(1), 87–128 (2014).

34. M. R. Lotz, C. R. Petersen, C. Markos, O. Bang, M. H. Jakobsen, and R. Taboryski, "Direct nanoimprinting of moth-eye structures in chalcogenide glass for broadband antireflection in the mid-infrared," *Optica* **5**(5), 557–563 (2018).
35. K. Kato, F. Tanno, and N. Umemura, "Sellmeier and thermo-optic dispersion formulas for GaSe (Revisited)," *Appl. Opt.* **52**(11), 2325–2328 (2013).
36. D. Brida, G. Krauss, A. Sell, and A. Leitenstorfer, "Ultrabroadband Er: fiber lasers," *Laser Photonics Rev.* **8**(3), 409–428 (2014).